Lung Self-Assembly Is Modulated by Tissue Surface Tensions

Margaret A. Schwarz[1], Haihua Zheng[2], Susan Legan[1], and Ramsey A. Foty[2]

[1]University of Texas Southwestern Medical Center at Dallas, Dallas, Texas; and [2]Robert Wood Johnson Medical School–University of Medicine and Dentistry of New Jersey, New Brunswick, New Jersey

To identify cell-intrinsic properties that facilitate interaction between epithelial endodermal and mesenchymal mesodermal cells during lung morphogenesis, we developed a model of lung self-assembly that mimics fetal lung formation in structure, polarity, vasculature, and extracellular matrix expression. Three-dimensional pulmonary bodies (PBs) spontaneously self-assemble from single-cell suspensions and exhibit liquid-like properties that allow measurements of compaction rate and cohesion, and that may help to specify cellular self-organization. We hypothesized that changes in one or more of these parameters could potentially explain the lung hypoplasia associated with abnormal lung development. We examined the impact of endothelial/monocyte–activating polypeptide (EMAP) II in PBs, because EMAPII is highly expressed in lung hypoplasia. EMAPII significantly increased compaction rate and decreased overall cohesion of PBs composed of both epithelial and mesenchymal cells. Moreover, the effects of EMAPII on compaction and cohesion act exclusively through the mesenchymal cell population by interfering with fibronectin matrix assembly. We also show that EMAPII alters epithelial cell polarity and surfactant protein C expression. Our findings demonstrate, for the first time, that PBs possess liquid-like properties that can help to guide the self-assembly of fetal lungs, and that EMAPII expression can influence both mesenchymal and epithelial cells but through different molecular mechanisms.

Keywords: cohesion; cell–cell interactions; polarity; extracellular matrix

Early lung morphogenesis, initiated by a series of genetic cues, is characterized by the evagination of the foregut epithelium into the underlying mesoderm. Using a stereotypic pattern of reproducible budding and branching events, a tree-like system of epithelial branches gives rise to the mature lung organ. In conjunction with epithelial branching, a complex vascular tree, comprised of vessels arising from angiogenic and vasculogenic mechanisms, establishes an alveolar and vascular interface capable of oxygen exchange. The proximity and interdependence of the distal lung alveoli and vasculature for progression of normal development underscore the importance of an adhesion-based mechanism capable of mediating these cellular interactions. For example, vascular overabundance in lung-specific surfactant protein C (SPC) promoter vascular endothelial growth factor transgenic mice is associated with abnormal branching morphogenesis and inhibition of type I cell differentiation (1). Antiangiogenic proteins also influence distal lung morphogenesis. For instance, endothelial/monocyte–activating polypeptide (EMAP) II has been shown to markedly decrease lung vasculature, induce distal lung hypoplasia, and inhibit distal epithelial cell differentiation in a fetal lung allograft model (2). Conversely, disruption of a gene associated with epithelial structural maturation, such as transforming growth factor–β1, results in vascular malformations in conjunction with the arrest of lung sacculation and epithelial cell differentiation (3, 4). Taken together, these studies suggest that distal alveolar morphogenesis and capillary formation are interdependent, and can be influenced by changes in both the vascular and cellular compartments. This study attempts to dissect the relative contributions of a vascular mediator on the cellular compartment to the process of lung morphogenesis.

CLINICAL RELEVANCE

This article is optimally suited for this venue, as it introduces a novel and exciting research tool that demonstrates the unique properties of the developing lung that are relevant to understanding morphogenesis.

The interconnected nature of the interaction between alveoli and the vasculature suggests that distal pulmonary organization is a dynamic process. Accordingly, a study of the mechanisms underlying distal pulmonary organization must be able to recapitulate and quantify the dynamic nature of the process. Recombinant lung coculture (5) or fetal lung tissue resuspended in Matrigel (6, 7) are reasonable approximations of lung development, but are limited inasmuch as they are not inherently quantitative in nature. To understand better the impact that cellular interactions have on lung development, we examined the ability of lung tissue to self-assemble in the three-dimensional (3D) environment of a hanging drop (HD). There is precedent for studying morphogenesis using dispersed embryonic tissues in 3D culture. For example, chick embryonic tissues, such as limb bud mesenchyme, heart, liver, and neural retina, when enzymatically dispersed, spontaneously reaggregate into spheres. Methods have been developed to exploit this ability to form spheroids. One such method, tissue surface tensiometry (TST), measures the cohesion between cells in these 3D tissue–like structures. In these studies, Foty and colleagues (8, 9) demonstrated that embryonic tissues have cohesive properties that are tissue type specific, and that are predictive of spatial organization between different tissue types. To understand better the intercellular dynamics of lung development, we measured the cohesivity of fetal lung spheroids and correlated cohesivity with self-assembly. We also explored the effects of EMAPII treatment on cohesivity and the self-assembly process.

Here, we show that dissociated fetal lung cells possess an innate ability to self-assemble into structures that replicate fetal lung structure in the pseudoglandular stage in organization, polarity, and extracellular matrix (ECM) deposition. Using fetal lung aggregates, termed pulmonary bodies (PBs), we measured cohesivity by TST and determined that PBs have liquid-like

(*Received in original form August 21, 2009 and in final form June 18, 2010*)

This work was supported in part by National Institutes of Health grants HL-60061 and HL-75764 (M.A.S.) and CA118755 (R.A.F.).

Correspondence and requests for reprints should be addressed to Margaret A. Schwarz, M.D., UT Southwestern Medical Center at Dallas, 5323 Harry Hines Boulevard, Dallas, TX 75390-9063. E-mail: margaret.schwarz@utsouthwestern.edu

This article has an online supplement, which is accessible from this issue's table of contents at www.atsjournals.org

Am J Respir Cell Mol Biol Vol 44. pp 682–691, 2011
Originally Published in Press as DOI: 10.1165/rcmb.2009-0309OC on July 8, 2010
Internet address: www.atsjournals.org

properties that could be exploited to generate measurements of intercellular binding energy (10). As previous studies have shown that EMAPII profoundly disrupts alveolar capillary growth, and is highly expressed in lung hypoplasia, we examined the impact of EMAPII on lung self-assembly and cohesivity. We determined that PBs cellular self-organization and cohesivity are significantly altered by EMAPII via an fibronectin (FN) matrix–mediated mechanism. Furthermore, we identified that combined endoderm and mesoderm–derived cell type PBs respond differently to EMAPII treatment with regard to aggregation rate and effect on cohesivity.

MATERIALS AND METHODS

Cell Culture

Chinese hamster ovary cells. Chinese hamster ovary (CHO) X5C5 express α5β1-integrin. Cells were maintained in Dulbecco's modified Eagle's medium (Invitrogen, Carlsbad, CA) containing 10% FCS (HyClone Laboratories, Logan, UT), 2 mM glutamine, 1% sodium pyruvate, 1% nonessential amino acids, 1% antibiotics/antimycotics, and 200 μg/ml G418. Cell surface expression of α5β1 was verified by flow cytometry to ensure stable integrin expression.

PB Formation and Compaction

Fetal lungs were microdissected from timed-pregnant mice at Embryologic Day (E) 14.5. The tracheas were removed and lung tissue was finely minced and dissociated with 0.5% collagenase (Invitrogen) and 20 μg/ml DNase1 (Sigma-Aldrich, St. Louis, MO). After centrifugation, the cells were suspended in red blood cell lysis buffer (Sigma-Aldrich), rinsed in PBS, and passed through a 100-micron filter. Single cells were then counted and suspended in Dulbecco's modified Eagle's medium with 20% FBS and 1% Penicillin/Streptomycin at a concentration of 1×10^7 cells/ml. Viability using Trypan blue exclusion indicates that greater than 95% of the cells are viable at this point. Aliquots (12.5 μl) were deposited on the underside of the lid of a 10-cm tissue culture dish. The bottom of the dish contained 5 ml of PBS and served to prevent evaporation of the drops by forming a hydration chamber. HDs were created by inverting the lid over the hydration chamber. The drops were incubated at 37°C, 5% CO_2, and 95% humidity for 2 days, allowing cells to coalesce and form cell sheets. Compaction was monitored over 48 hours. Some HDs were treated with vehicle, EMAPII (3 μg/ml), or 70-kD fragment of fibronectin (FN). After 48 hours in HDs, PB compaction was assessed as previously described (10–12, 13). Briefly, phase–contrast images of compacted aggregates were captured, and each image was adjusted to optimize contrast. Aggregate images were then assigned a false color, and outlines were automatically traced by the image analysis software. Measurements of the number of pixels contained within each outline were generated. This method provides a quantifiable assessment of PB size. After measurement, the aggregates were transferred to 10-ml shaker flasks. Flasks were placed into a 37°C orbital shaker/5% CO_2 incubator at 130 rpm, and cohesion analyzed at 24, 48, and 72 hours by TST. In some studies, epithelial and mesenchymal cell populations were isolated using differential adhesion techniques, as previously described (14, 15). In brief, once a single suspension of cells was obtained, cells were plated on tissue culture plates for 30 minutes, with the first cell population to attach being the mesenchymal cells. The nonadherent cells after a second 1.5-hour plating were identified as the epithelial cell population. The cells that attached in the second plating were a mixed cell population.

TST

After 24–72 hours in the orbital shaker, the cohesivity of control and EMAPII-treated PB aggregates was measured by TST, as previously described (8, 9). Briefly, spherical aggregates ranging in size from 200–300 μm in diameter were transferred to the inner chamber of the tissue surface tensiometer and positioned on the lower compression plate (LCP). The inner chamber contains prewarmed, degassed, CO_2-independent medium (Gibco-BRL, Carlsbad, CA) supplemented with 10% FCS and antibiotics. The upper compression plate (UCP), attached to a nickel-chromium wire, was then positioned above the aggregate and connected to a Cahn electrobalance (Cahn Instruments, Cerritos, CA). The weight of the UCP was zeroed to establish a precompression UCP weight baseline value. To minimize adhesion of cell aggregates to the compression plates, both the lower and upper plates were precoated with poly-2-hydroxyethylmethacrylate (Sigma-Aldrich), a polymeric material to which cells do not adhere (16). Compression was initiated by raising the LCP until the aggregate became compressed against the UCP. Adjusting the height of the LCP controls different degrees of compression. The force with which the aggregate resists compression was monitored by the Cahn recording electrobalance. Aggregate geometry was monitored using a Nikon dissecting microscope (Melville, NY) equipped with a CCD video camera (Sony Corporation, Tokyo, Japan) and connected to a computer with a frame-grabber. Images of aggregates were captured, digitized and their geometries analyzed using NIH Image software (National Institutes of Health, Bethesda, MD). Each aggregate was subjected to two different degrees of compression, the second greater than the first. Measurements of aggregate geometry and the force of resistance to the compressive force were then used to solve the Young-Laplace equation (17), producing numerical values of apparent tissue surface tension (σ).

Envelopment Assays

After lung dissociation, single-cell suspensions were stained with either PKH26 Red Fluorescent General Cell Linker or with PKH2 Green Fluorescent General Cell Linker (Sigma-Aldrich), as recommended by the manufacturer. Stained cells were used to form separate spheroids either in the presence or absence of EMAPII. Treated and untreated aggregates were fused in HD culture. After 48 hours, fused aggregates were fixed in 2% paraformaldehyde in PBS and imaged with an Olympus IX81 microscope equipped with a DSU spinning disc confocal imaging system (Center Valley, PA). Images were captured using a Sensicam QE CCD camera (Cooke Corp., Eugene, OR). Black and white images were captured for each of the two channels, pseudocolored, and merged to reveal the configurations generated.

Immunoblot Analysis

Cells were lysed in 50 mM Tris (pH 7.4), 0.9 N NaCl, 1% NP-40, and 0.01% NaN3, in the presence of the protease inhibitors (aprotinin 20 μg/ml, leupeptin 20 μg/ml, and pepstatin A 20 μg/ml), and stored at −70°C. Homogenates were cleared by centrifugation at $14{,}000 \times g$ for 20 minutes, the protein concentration determined by Bradford analysis (Bio-Rad, Hercules, CA), and the samples normalized by protein content. Equal amounts of protein were electrophoresed on a 10% SDS-PAGE gel, transferred to Immobilon-P membranes, blocked overnight in a casein-based blocking solution (Boehringer-Mannheim, Indianapolis, IN), and probed with primary antibodies against Pan-cadherin, proliferating cell nuclear antigen, or actin (Sigma-Aldrich). Specific binding was detected using a chemiluminescence substrate (Pierce, Rockford, IL) and XAR-5 film (Eastman Kodak, Rochester, NY). Quantitative analysis was accomplished using Quantity One Software (Bio-Rad Laboratories, Hercules, CA) and samples were normalized to actin.

To detect insoluble and soluble FN, PBs were incubated for either 1 or 3 days in HD culture, then pooled and lysed in a deoxycholate (DOC) lysis buffer (2% sodium deoxycholate, 0.02 M Tris-HCl [pH 8.8], 2 mM PMSF, 2 mM EDTA, 2 mM iodoacetic acid, and 2 mM *N*-ethylmaleimide), passed through a 26-gauge needle, and centrifuged at $15 \times g$ for 20 minutes at 4°C. The supernatant containing the DOC-soluble component was separated and then pelleted by centrifugation. DOC-insoluble components were solubilized using SDS lysis buffer (1% SDS, 25 mM Tris-HCl [pH 8.0], 2 mM PMSF, 2 mM EDTA, 2 mM iodoacetic acid, and 2 mM *N*-ethylmaleimide). Reduced lysates were separated on SDS-PAGE gels and probed with an anti-FN antibody (ab6584; AbCam, Ltd., Cambridge, UK). Under reducing conditions, high–molecular weight FN multimers resolve as a 220-kD band. Semiquantitative densitometry was performed as previously described (10).

Histological Analysis

PBs were rinsed in PBS, fixed in 4% paraformaldahyde, and placed in 30% sucrose before being mounted in OCT (optimal cutting temper-

ature compound). Cryostat sections were permeabilized with 0.1% Triton-X100, rinsed with PBS, blocked using CAS Block blocking buffer (Zymed, San Francisco, CA), and exposed to the primary antibody for 1 hour (laminin α [ab30320; Abcam], PECAM-1 (platelet endothelial cell adhesion molecule-1) [553370; BD Pharmingen, San Diego, CA], zona occludens [ZO]–1 [40–2300; Zymed]; SPC [07-647; Upstate, Lake Placid, NY], FN [ab23750; Abcam], collagen I [ab21286; Abcam], activate caspase 3 [AB3623; Chemicon, Temecula, CA]), smooth muscle actin (SMA), Golgi marker (GM130), per the manufacturers' instructions. After washing with PBS, tissues were exposed to the appropriate secondary Cy3 or AlexaFluor 488 fluorescent antibody (Chemicon and Molecular Probes/Invitrogen) for 1 hour. For dual localization, primary antibodies from different species were incubated together while primary antibodies from same species were performed separately after repeated blocking and a separate incubation period. This was followed by a 6-minute incubation with membrane-permeable 4′,6-diamidino-2-phenyindole (5 mg/ml at 1:1,000 dilution; Sigma-Aldrich), rinsing with PBS, and mounting. Actin was detected by phalloidin-FITC staining. Fluorescent signals were detected by fluorescence microscopy at the appropriate wavelength for the secondary antibody on an IX81 Olympus microscope, and images captured with a Hamamatsu Orca digital camera (Hamamatsu Corporation, Bridgewater, NJ) with a DSU spinning confocal unit using Slidebook software (Intelligent Imaging Innovations, Philadelpha, PA).

Statistical Analysis

Statistical analysis was performed, where appropriate, by Student's *t* test, ANOVA/Newman-Keul's or Tukey's Honestly Significant Difference, or by linear regression, using PRISM 4.0 for MacIntosh statistical analysis software (GraphPad Software, Inc., San Diego, CA).

RESULTS

Dissociated Fetal Lung Cells Spontaneously Form Spheres in HD Cultures

Coherent mobile cells will often spontaneously rearrange into spheres in order for the individual cell populations to maximize their mutual bonding and minimize adhesive free energy (18). This liquid-like behavior can be exploited to generate measurements of intercellular binding energy, expressible as σ. Previous studies have shown that individual 3D alveolar forming units can be engineered by incubating cells in the presence of a Matrigel hydrogel or synthetic polymer scaffolds (6). We asked whether heterogenous cell populations of fetal lung could rearrange in the absence of an exogenous matrix scaffold. This ability would make it possible to generate measurements of intercellular binding energy. Dissociated single-cell E14.5 lungs from the mid-pseudoglandular stage were placed in HD cultures and examined for their ability to form spheres (Figure 1). In the absence of artificial matrices, fetal pulmonary cells, placed in a 3D HD, aggregated to the center of the drop by 20 hours (Figure 2A) and formed sheets of cells. After 48 hours, the 3D pulmonary sheets formed spherical aggregates that remained intact as they were transferred to a shaker flask. The surface tension of these spheres was then measured by TST.

PB Spheres Have a Measurable Surface Tension

Previous studies have shown that embryonic tissues possess markedly different cohesive properties, which govern their spatial relationship (8, 9, 19). We measured the surface tension of PB aggregates, and found them to be quite cohesive, with a σ value of 19.9 (±1.3) dynes/cm ($n = 14$). This cohesivity compares with that of embryonic chick limb bud mesenchyme, considered to be one of the more cohesive embryonic tissues measured, as the measured surface tensions of the lung tissues studied (10–20 dynes/cm) fall in the same range as surface tensions of normal chick embryonic tissues (1.5–25 dynes/cm), as demonstrated by Foty and colleagues (9). We validated our surface tension measurements by demonstrating that σ was both size and force invariant, as previously described (10): for a liquid system, the ratio of σ measured at two successive and greater compressions must be approximately 1.0. As shown in Table 1, the ratio for untreated PBs was 1.058, and was consistent with liquid-like behavior. Moreover, cohesivity must also be size independent. As can be seen in Figure 3B, linear regression analysis showed that surface tension was independent of PBs size ($r^2 = 0.0008$).

Dissociated fetal lungs self-assemble in PBs with the same histotypic organization as normal lung tissue. Earlier studies suggested that, in 2D culture, fetal lung cells retain an innate ability to cluster epithelial cells within a surrounding mesenchyme (5, 20–22), whereas the presence of a 3D Matrigel or a synthetic polymer scaffold gives rise to alveolar cyst formation (6). Analysis after 48 hours in the shaker bath indicated that the round PBs were histologically similar to fetal lung in the pseudoglandular stage. PBs demonstrated epithelial cell apical/basilar polarity, as determined by ZO-1 distribution on the apical region (Figures 2D and 2E) ($n = 5$) and laminin ECM

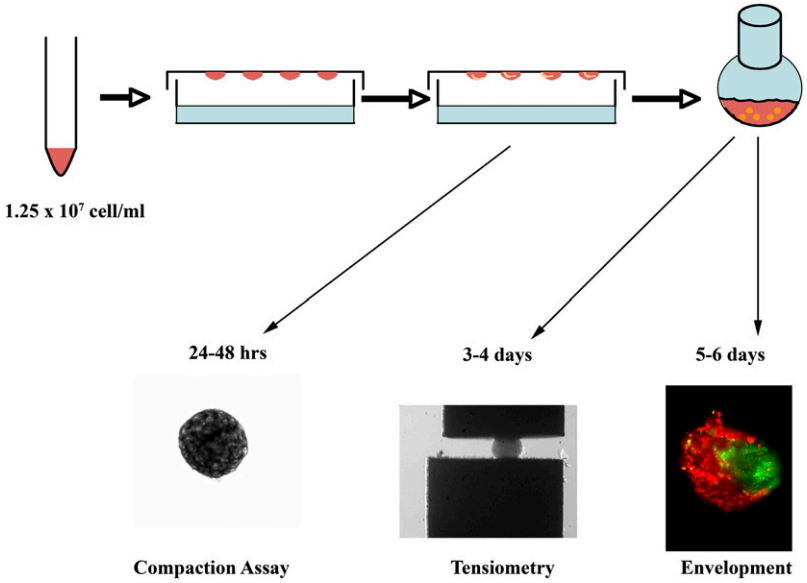

Figure 1. Fetal pulmonary cells in three-dimensional (3D) suspension self-assemble to form pulmonary bodies (PBs). Fetal lungs isolated at Embryologic Day 14.5 were enzymatically dissociated and resuspended in 3D hanging drops (HDs). Pulmonary cells (1.25×10^7 cell/ml) self-assembled or compacted over 48 hours to form pulmonary sheets (compaction assay). Pulmonary sheets placed in a shaker flask for 24–48 hours formed spherical PBs. These were subjected to tissue surface tensiometry (TST) to measure aggregate cohesivity (tensiometry), or to envelopment assays in which pairs of differentially stained PBs were apposed in 3D HDs and examined by fluorescence microscopy after 24–48 hours (envelopment).

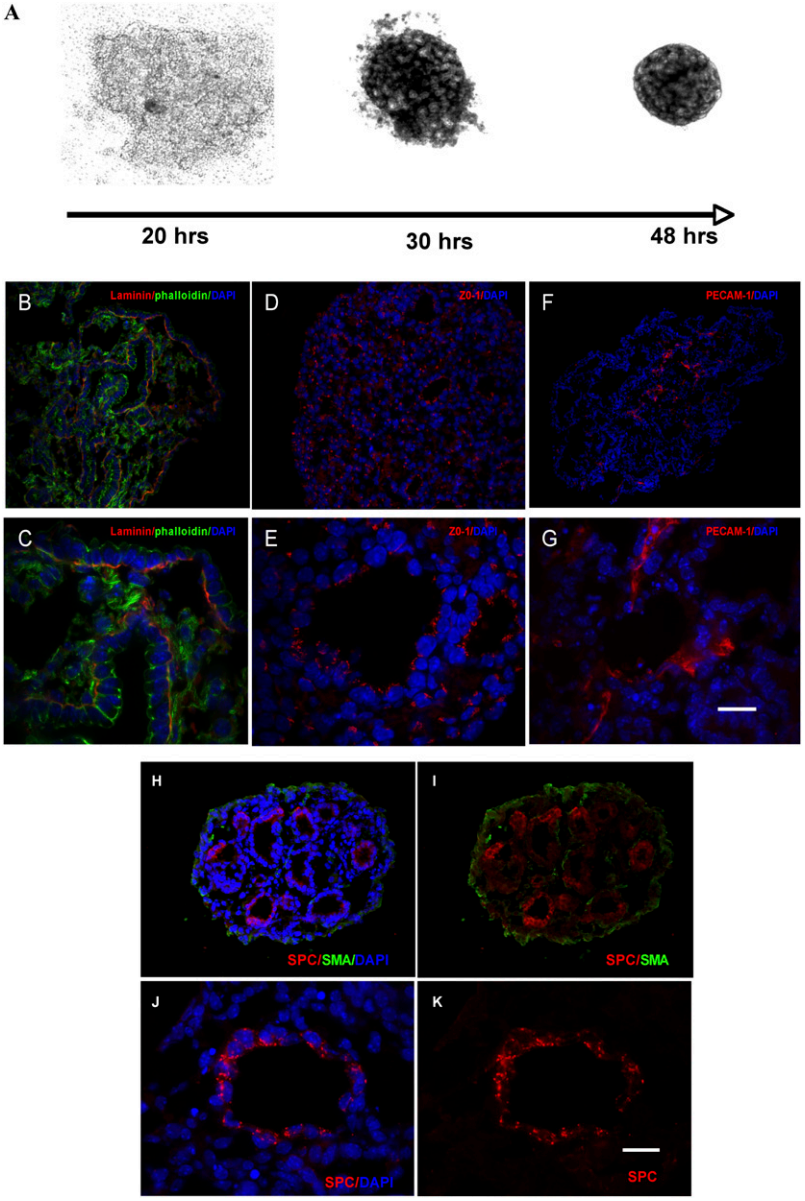

Figure 2. PBs form blood vessels, polarize epithelial cells, and express surfactant protein C (SPC). Dissociated fetal lung cells aggregate over 48 hours to form sheets (*A*). After orbital shaking for 24–48 hours, immunofluorescent analysis of PBs indicate that laminin α (*B* and *C*) (cy3, FITC-phalloidin) localized to the basilar surface of the epithelium at the epithelial–mesenchymal interface, zona occludens (ZO)–1 expression was confined to the apical region of the epithelial cyst (*D* and *E*), as demonstrated by their SPC expression (*H–K*) (cy3, FITC-SMA), and platelet endothelial cell adhesion molecule-1 (PECAM-1) distribution was confined to the mesenchyme (*F* and *G*). DAPI, 4′,6-diamidino-2-phenyindole (denotes nuclear staining) (*B–H* and *J*). *Scale bar*, 60 μm (*B*, *D*, *F*, *H*, *I*) and 20 μm (*C*, *E*, *G*, *J*, *K*).

deposition on the basilar region (Figures 2B and 2C) ($n = 5$). Furthermore, SPC (Figures 2H–2K) ($n = 4$) was confined to the epithelial cells, whereas lace-like PECAM-1–positive cells were limited to the SPC-negative regions consistent with mesenchyme (Figures 2F and 2G) ($n = 4$).

EMAPII treatment results in an increase in aggregate compaction. To determine whether cell–cell interactions mediate fetal lung assembly and cohesion, dissociated fetal lung cells were exposed to either vehicle or the antiangiogenic protein, EMAPII, as previous studies have shown that EMAPII profoundly disrupts alveolar capillary growth, and is highly expressed in lung hypoplasia (2, 23). Aggregation or compaction were assessed after 48 hours in HDs. As can be seen in Figure 3A, HDs treated with EMAPII were significantly smaller at 48 hours ($5.45 \pm 0.4 \times 10^7$ pixels) than untreated controls ($7.09 \pm 0.36 \times 10^7$ pixels) ($P = 0.0038$, Student's t test; $n = 10$; Figure 3A). This difference in aggregate size may have arisen due to either a faster rate of compaction or to an EMAPII-induced increase in aggregate cohesivity. To differentiate between these two possibilities, we measured the cohesivity of EMAPII-treated and control PBs by TST.

EMAPII decreases PB cohesivity and alters envelopment behavior. EMAPII-treated PBs readily formed spheroids and were liquid-like ($\sigma_2/\sigma_1 = 1.034$, Table 1). Their cohesivity, however, was markedly decreased ($\sigma = 13.47 \pm 1.455$ [SEM]; $P = 0.0002$, Student's t test) as compared with control ($\sigma = 19.97 \pm 1.346$ [SEM]) ($n = 14$) (Figures 3C and 3D; Table 1). This decrease in aggregate cohesion could, in principle, give rise to the increase in the observed compaction rate by reducing the effective viscosity of the aggregate. Previous studies have shown that tissue cohesion can strongly influence the relative spatial position adopted by different cell populations in mixed tissues. We performed envelopment assays to determine whether EMAPII's ability to decrease PB cohesion results in differential envelopment behavior. Using cell surface intercalating dyes to mark differently treated populations (EMAPII versus control), spheroid PB aggregates were placed in apposition in a 3D HD. Consistent with their lower cohesivity, EMAPII-treated PBs enveloped the untreated control PBs (Figures 3G and 3H). No envelopment was noted in PBs with similar cohesivity (control/control [Figure 3E], EMAPII/EMAPII [Figure 3F]). These data

TABLE 1. AGGREGATE SURFACE TENSION VALUES FOR CONTROL AND ENDOTHELIAL/MONOCYTE–ACTIVATING POLYPEPTIDE II–TREATED PULMONARY BODY AGGREGATES

Treatment	σ_1 (*Dynes/cm*)	σ_2 (*Dynes/cm*)	P σ_1 vs. σ_2	$\sigma_{1,2}$ (*Dynes/cm*)	σ_2:σ_1 (*Dynes/cm*)
Control	19.42 ± 1.944	20.56 ± 1.915	0.6788	19.97 ± 1.346	1.058
EMAPII	12.66 ± 1.252	13.10 ± 2.134	0.8551	13.47 ± 1.455	1.034

Definition of abbreviations: EMAP, endothelial/monocyte–activating polypeptide; σ, apparent tissue surface tension.

σ_1 and σ_2 represent the respective surface tensions for first and second compressions, and $\sigma_{1,2}$ is the average. We validated the surface tension measurements by showing that σs measured for two different degrees of compression are not statistically different (Student's *t* test, $P > 0.05$), and that the ratio of surface tension (σ_2:σ_1) for two successive compressions approaches 1.

suggest that EMAPII engenders a decrease in cohesivity that may influence the ability of cells to adopt their appropriate spatial relationships, in turn leading to alterations in lung morphology. We next explored a potential molecular mechanism underlying EMAPII-induced decrease in PB cohesivity.

EMAPII disrupts FN matrix assembly in PBs. Previous studies have shown that α5β1-integrin–FN interaction can markedly increase aggregate cohesion (11), and that FN matrix assembly is an important regulator of this process (10, 11). Other studies indicate that FN matrix assembly is inhibited by EMAPII via a direct interaction with α5β1-integrin (24). To determine if EMAPII's inhibition of FN matrix assembly and cohesion in PBs was mediated by an α5-integrin mechanism, we first used a model system in which α5β1-integrin–Fn interaction was the principle adhesion system. CHO cells null for endogenous α5-integrin were generated to express human α5-integrin (CHOα5) (10) on the cell surface. Similar to prior studies where inhibition of FN matrix in CHOα5 cells inhibited aggregate formation, EMAPII significantly repressed CHOα5-mediated aggregate compaction ($P = 0.0001$, Student's *t* test; Figure 4A) ($n = 10$). We next examined PB sphere formation to determine if FN matrix assembly mediates cell–cell interactions in this mixed cell population. Using a strategy that allows α5β1-integrin receptor engagement, but inhibits intracellular signaling, we used a truncated form of FN, the 70-kD FN fragment. Binding of the 70-kD FN fragment results in the nonfunctional binding of the α5β1 receptor, but lacks the functional cellular signaling due to its smaller size resulting in a reduction of insoluble FN deposition. Addition of 12.5 μg/ml of the 70-kD FN fragment resulted in a significant decrease in PB aggregate size as compared with controls. Interestingly however, higher concentrations of the 70-kD FN fragment (12.5–100 μg/ml) resulted in a linear increase

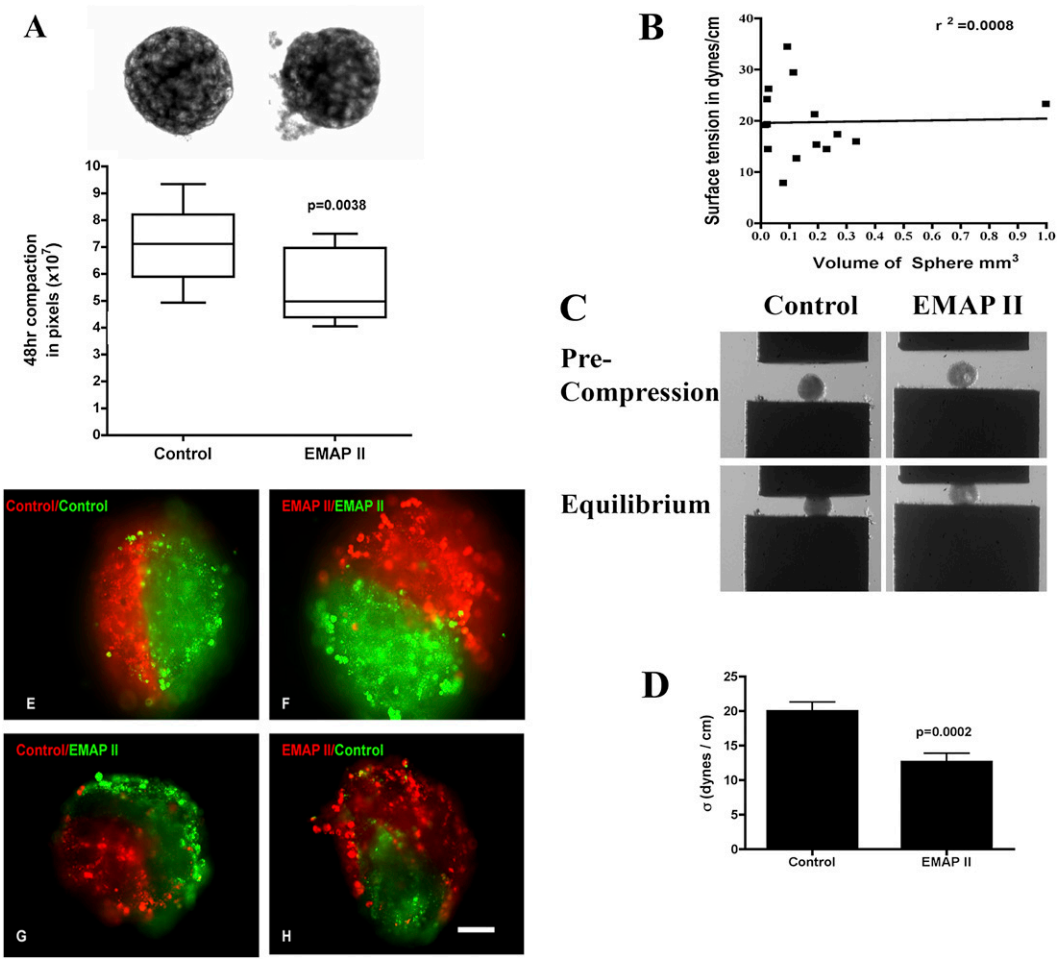

Figure 3. Pulmonary sheet compaction is accelerated by endothelial/monocyte–activating polypeptide (EMAP) II, whereas cohesivity is decreased. The assembly of dissociated fetal lung cells into an aggregate within 48 hours into pulmonary sheets was assessed. HDs treated with EMAPII exhibited a more rapid rate (A) of compaction as compared with controls ($P = 0.0038$, Student's *t* test, representative experiment performed at least 10 times). Magnification, 100×. PBs subjected to TST were noted to have liquid properties and surface tension that, by linear regression, was shown to be independent of aggregate size (*B*) (r^2=0.0008). (*C*) PB aggregates at precompression (*top panels*) and after PBs have reached force and shape equilibria (*bottom panels*). PB cohesivity was markedly decreased in aggregates treated with EMAPII as compared with controls (*D*) ($P = 0.0002$; $n = 14$). Dissociated fetal lung cells were stained with membrane intercalating green or red fluorescent dyes. After formation, PBs were fused in 3D HDs and envelopment assessed. The less cohesive EMAPII-treated PBs enveloped the more cohesive untreated PBs (*G* and *H*). Combinations in which like-aggregates were used fused along their midline and formed a planar interface (*E* and *F*). *Scale bar*, 40 μm.

in aggregate size ($P = 0.001$, Tukey's multiple comparison test) (ANOVA, $P = 0.0001$; Bartlett's, $P = 0.0001$; Figure 4B), demonstrating that blocking matrix assembly by the 70-kD fragment markedly reduced compaction of PBs. Lastly, to determine if FN matrix assembly was mediated by EMAPII in PB formation, FN matrix assembly was assessed using immunofluorescence microscopy and a DOC differential solubilization assay, followed by immunoblot analysis. EMAPII markedly reduced FN matrix assembly ($P = 0.009$, Student's t test; $n = 6$; Figures 5B and 5C) in PBs as compared with control (Figures 5A and 5C). As FN provides the initial provisional matrix that facilitates subsequent matrix formation, we examined whether other matrix formation was impacted by its reduction. Consistent with a loss of FN matrix assembly, there was a marked decrease in deposition of the structural protein, collagen 1, at the epithelial–mesenchymal interface in EMAPII-treated PBs (Figure 5E) as compared with controls (Figure 5D). In contrast to a marked reduction in FN matrix assembly, EMAPII did not alter pan-cadherin or metalloproteinase expression, as noted by Western blot analysis and zymograms (data not shown). To define more clearly the effect of EMAPII on FN matrix assembly, we asked whether EMAPII specifically targets the endodermal (epithelium) or mesodermal (mesenchyme) subpopulations of cells within PBs.

EMAPII specifically targets the mesodermal component of the PBs. We isolated mesenchymal and epithelial cells, and incubated each population in EMAPII. Aggregate compaction was then assessed. As shown in Figure 6B, mesenchymal cells rapidly assembled into compact mesenchymal bodies (MBs), with volumes that ranged from 0.0042 to 0.0287 ($\pm$0.0089) mm^3. Importantly, linear regression analysis showed that surface tension was independent of aggregate size (r^2=0.046; $n = 10$; Figure 6B). In contrast, epithelial cells did not aggregate over the same 48-hour period, and remained as sheets of loosely associated cells (data not shown). As the epithelial cells did not aggregate, EMAPII had little impact on compaction. In contrast, compaction was inhibited in mesenchymal cells treated with EMAPII ($P = 0.014$, Student's t test; $n = 10$; Figure 6A). We assessed the effects of EMAPII treatment on the mesenchymal

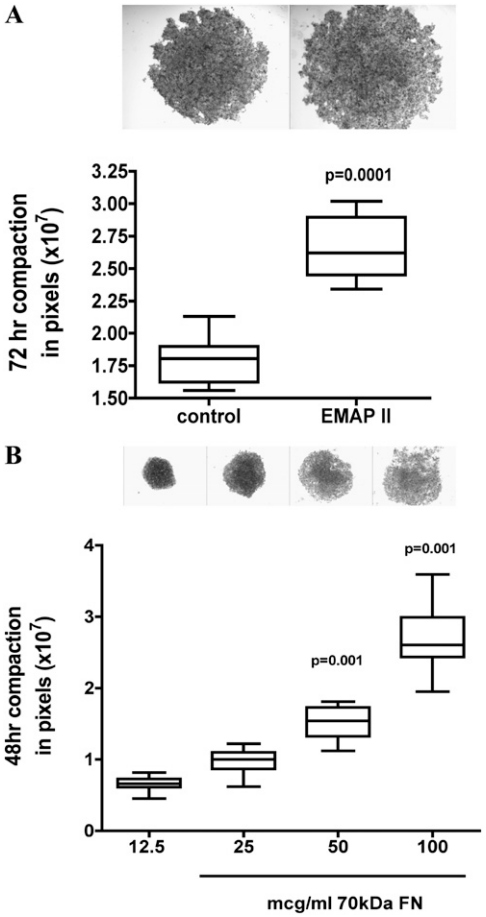

Figure 4. Disruption of fibronectin (FN) matrix assembly alters compaction in α5-integrin expressing Chinese hamster ovary (CHO) cells and in PBs. CHO-α5 cells in 3D HDs treated with EMAPII had a marked suppression in compaction as compared with controls ($P = 0.0001$, representative experiment $n = 10$, performed 3 times). PBs treated with the 70 kD fragment of FN had a dose-dependent near-linear relationship in compaction with higher doses (50–100 μg/ml; $P = 0.05$ and 0.001, respectively) inhibiting compaction (representative experiment $n = 10$, performed three times).

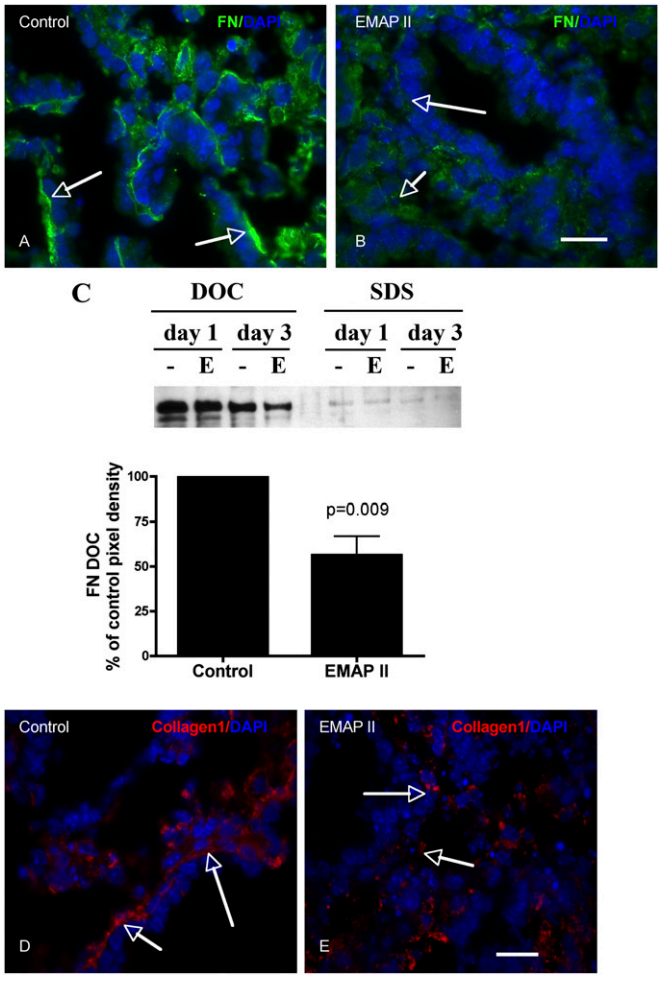

Figure 5. EMAPII inhibits PBs fibrillogenesis and collagen I deposition in PBs. Fibrillogenesis was assessed in PBs treated with EMAPII. Immunofluorescence analysis indicates that EMAPII inhibits insoluble FN matrix deposition, as noted by the lack of insoluble FN strands at the epithelial/mesenchymal interface (*B*) (FN–FITC, *arrows*) as compared with the insoluble strands of FN noted in controls (*A*) (*arrows*). Isolation of insoluble deoxycholate (DOC) FN supports this observation, as EMAPII (*C*) (*lane E*) suppressed the insoluble form of FN ($P = 0.009$) (*C*) ($n = 6$; *lane* marked with *dash*). Collagen I deposition was also altered by EMAPII (*E*) (*arrows*, Cy3) as compared with controls (*D*) (*arrows*). DAPI denotes nuclear staining (*A*, *B*, *D*, *E*). *Scale bar*, 20 μm.

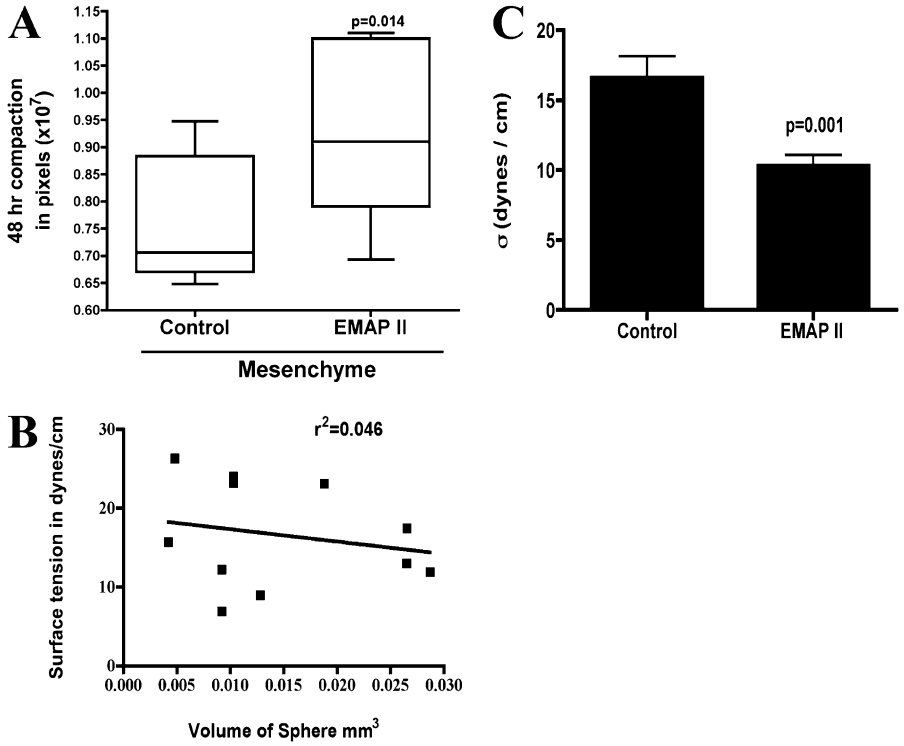

Figure 6. Mesoderm compaction and cohesivity is inhibited by EMAPII, whereas endoderm compaction is not. Aggregate formation was examined in isolated epithelial and mesenchymal cells. Mesenchymal sheet compaction was significantly inhibited by EMAPII (*A*) ($P = 0.014$, $n = 10$, representative experiment, performed 10 times) as compared with controls. Mesenchymal bodies (MBs) subjected to TST were noted to have liquid properties and surface tension that was independent of aggregate size (*B*) ($r^2 = 0.046$). MB cohesivity was markedly decreased in aggregates treated with EMAPII as compared with controls (*C*) ($P = 0.001$, $n = 10$).

cell population. Similar to our observations on PBs, EMAPII significantly reduced cohesivity of MBs from 20.10 (±3.011) dynes/cm to 9.7 (±1.0) dynes/cm (Table 2; Figure 6C). The surface tension values reported are for those aggregates within the data set displaying liquid-like properties where σ_2/σ_1 was approximately 1.0. EMAPII treatment had another interesting effect on aggregate biomechanical properties. Whereas untreated aggregates exhibited predominantly elastic-like properties, treated aggregates were predominantly liquid. That is, the ratio of σ_2:σ_1 of untreated aggregates was found to be 1.3, whereas that of EMAPII-treated aggregates was 1.02. Moreover, the number of liquid-like aggregates within each data set increased from 20% in untreated to 60% in the EMAPII-treated samples. Similar to PBs, EMAPII decreased FN matrix assembly in MBs by 25% versus controls, whereas pan-cadherin and metalloproteinase expression were unchanged (data not shown). These data suggest that EMAPII specifically targets the mesenchymal population by interfering with FN matrix assembly, thereby reducing overall tissue cohesivity. This change in cohesivity may influence cell–cell interactions underlying distal lung hypoplasia.

EMAPII inhibition of FN matrix assembly results in a loss of epithelial cell polarity. The ECM mediates renal epithelial polarity and differentiation (25, 26). In addition, presence of FN in the matrix has been associated with distal pulmonary epithelial cell cytoskeletal organization and polarization. As FN matrix assembly and collagen I deposition were inhibited in PBs treated with EMAPII, we examined whether epithelial cell polarity was altered. Histological analysis of expression of the apical markers, ZO-1 and GM130, suggests that PBs treated with EMAPII have a loss of epithelial cell apical alignment manifested by random cellular localization of ZO-1 and GM130 protein (Figures 7D–7F) as compared with the apical ZO-1/GM130 noted in control epithelial cells (Figures 7A–7C). In conjunction with loss of apical alignment, EMAPII-treated epithelial cell cysts were less complex, and collapsed into smaller aggregates as compared with controls (data not shown). In some instances, alterations in proliferation and apoptosis have been associated with a loss of apical alignment and FN matrix assembly. Western blot analysis of proliferating cell nuclear antigen (data not shown) and immunofluorescent analysis of active caspase 3 (*see* the online supplement) suggests that EMAPII inhibition of FN matrix assembly and polarity does not alter proliferation or apoptosis in PB assembly.

DISCUSSION

Here, we demonstrate that the multi–cell type fetal lung, in the absence of a gelatin, or Matrigel matrix, has the unique capacity of *de novo* 3D self-assembly. Lung tissue from E14.5 fetal mice, when dissociated and placed in shaking culture, reassemble into phenotypic pseudoglandular PBs that demonstrate typical lung histology, including epithelial cell polarity, ECM deposition, SPC expression, and lattice-like vessel formation. Reassembled PBs spontaneously form spheroids when placed in shaking tissue culture. This liquid-like behavior allows for measurement of their intercellular binding energy, otherwise expressed as tissue or aggregate cohesivity. Our data demonstrate that PB cohesivity is unexpectedly regulated by the antiangiogenic

TABLE 2. AGGREGATE SURFACE TENSION VALUES FOR CONTROL AND ENDOTHELIAL/MONOCYTE–ACTIVATING POLYPEPTIDE II–TREATED MESENCHYMAL AGGREGATES

Treatment	σ_1 (*Dynes/cm*)	σ_2 (*Dynes/cm*)	P σ_1 vs. σ_2	$\sigma_{1,2}$ (*Dynes/cm*)	σ_2:σ_1 (*Dynes/cm*)
Control	19.22 ± 4.743	20.98 ± 4.391	0.269	20.10 ± 3.011	1.092
EMAPII	9.100 ± 1.629	10.31 ± 1.391	0.220	9.700 ± 1.030	1.132

Definition of abbreviations: EMAP, endothelial/monocyte–activating polypeptide; σ, apparent tissue surface tension.

σ_1 and σ_2 represent the respective surface tensions for first and second compressions and $\sigma_{1,2}$ is the average. We validated the surface tension measurements by showing that σs measured for two different degrees of compression are not statistically different (Student's *t* test, $P > 0.05$), and that the ratio of surface tension (σ_2:σ_1) for two successive compressions approaches 1.

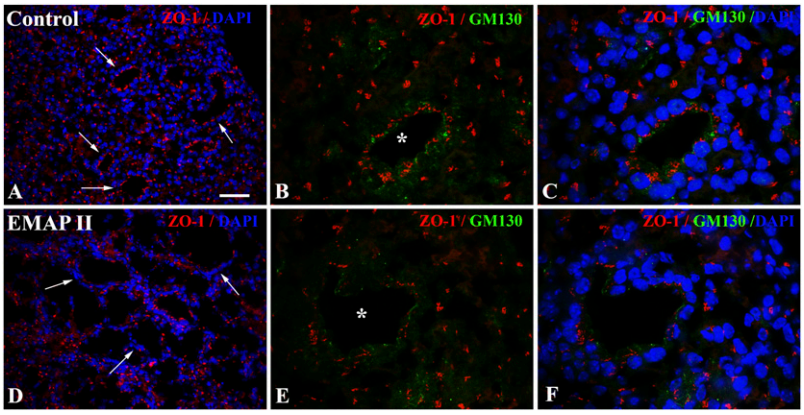

Figure 7. EMAPII alters epithelial apical alignment. PBs treated with EMAPII showed disrupted epithelial apical distribution of ZO-1 (*D–F*) (*arrow*, Cy3) and GM130 (*E* and *F*) (*asterisk* indicates epithelial cluster, FITC) as compared with controls (*A–C*) (*arrow* and *asterisk*). DAPI denotes nuclear staining (*A* and *B*). *Scale bar*, 50 μm (*A* and *D*) 16 μm (*B*, *C*, *E*, *F*).

protein, EMAPII (27, 28). EMAPII, a cleavage product of cell surface–expressed EMAPII protein (p43) (29), inhibits the interaction of α5β1-integrin with FN, resulting in a loss of FN deposition and fibrillogenesis (24). Inhibition of multicell PB fibrillogenesis by EMAPII enhances the rate of PB compaction, while reducing overall cohesivity. In contrast, both compaction and cohesivity were decreased by EMAPII in mesodermal cell populations, suggesting that EMAPII specifically acts through the mesenchymal cell component. These studies suggest that self-assembly may contribute to the process of lung development, and may be influenced by the expression and function of antiangiogenic proteins through an adhesion-based mechanism.

We used TST to assess changes in aggregate cohesion. This method has been previously described in detail (10–12, 13), and is also presented here as supplemental material. In brief, TST measures the intercellular binding energy of 3D spherical tissue aggregates under physiological conditions. We also employed an assay in which we measured the rate of compaction of cells in HD culture. Whereas TST measurements are predicated on the use of spherical aggregates, compaction assays measure the change in size of irregular flat sheets of cells. In this study, we chose to use an image analysis protocol in which high-contrast aggregate images were captured, their perimeter automatically delineated, and the number of pixels contained within the perimeter counted. Volumetric measurements were not possible, as: (*1*) aggregates did not assume shapes that conformed to those for which standard volumetric equations could be used; or (*2*) no z-axis information was captured to allow for calculation of accurate volumetric data. Measurement of aggregate area was also difficult, given the irregular shape of the aggregates, and would require multiple measurements of aggregate diameter and averaging, thus introducing measurement error. Accordingly, we believe that counting pixels represents the most accurate and straightforward method to measure differences in the size of aggregates of irregular shape.

Although previous studies indicate that fetal lung resuspended in Matrigel are a reasonable proxy of lung development (6, 7), they cannot be readily exploited to generate measurements of direct intercellular adhesion. The PB surrogates generated in this study, however, lend themselves to mechanical assessment of tissue properties, such as compaction and cohesivity, the latter being a property that has been previously demonstrated to significantly influence how cells organize spatially. Cadherins (30) and α5-integrin–FN interaction (10, 11) have been found to be key elements in the regulation of tissue cohesivity, as they are able to generate strong intracellular adhesions. This study has also identified a role for cadherins and for integrin function *vis-à-vis* FN matrix assembly as important components of PB formation. However, the role of the ECM goes beyond merely that of a scaffold, as its' function as a signaling system has been well established (31). During cellular differentiation, ECM-facilitated signaling is also involved in mediating cell viability and differentiation. For example, differentiation progresses in a stepwise fashion involving cell–cell adhesion that is mediated by cell adhesion complexes and cytoskeleton organization, followed by the formation of apical and basolateral domains that impart polarity to cells. Similarly, renal epithelial cell differentiation arises from cells that sequentially establish polarity and nuclear organization based on cell–cell contacts (25, 26). This triggers the segregation of marker proteins that are found in designated apical and basal-lateral domains in mammary epithelial cells (32). After polarity designation, differentiating cells extend into the ECM. Our studies demonstrate that the PBs establish a basilar ECM consisting of, but not limited to, laminin, FN, and collagen I. Furthermore, in conjunction with the formation of the ECM, epithelial cells establish polarity, as indicated by apical alignment of ZO-1 and GM130 expression, and express SPC. These findings support the PB as a surrogate of lung formation.

Our observations, that PBs form spheroids and spontaneously self-assemble *in vitro*, offer a unique opportunity to explore the mechanisms underlying adhesive cellular interactions that mediate lung morphogenesis. Spheroid formation is a typical liquid behavior. The concept of tissue liquidity has been demonstrated to play a part in a wide range of events in embryogenesis (33–35), wound healing (35), and malignancy (30, 35–37), and the underlying principle has been used to guide efforts at tissue engineering (34, 35, 38–40). Embryonic tissues of avian, teleost, and amphibian origin have been shown to exhibit liquid-like behavior. This is a first demonstration that mammalian embryonic tissue also exhibits behavior typical of liquid systems. We measured a σ of PB aggregates of approximately 20 dyne/cm, indicating that PB cohesivity is quite similar to that measured for embryonic chick forelimb mesenchyme. Interestingly, during embryonic and early pseudoglandular stages, mouse lung is predominantly mesoderm. Indeed when we measured the specific σ for the lung mesodermal population, we found surface tension to be approximately 20 dyne/cm, indicating that most of the cohesion of the PBs arises as a result of mesenchymal cell cohesion. Because epithelial cells isolated from lung tissue did not form spheres, we could not directly measure σ. Accordingly, it is likely that epithelial cell cohesion is relatively weak, and that much of the cohesion of the PBs is of mesodermal origin. Indeed, when mesenchymal cells were isolated from lung cultures, they readily formed spheres with a measured surface tension of approximately 20 dynes/cm. This led us to speculate that alteration in the overall cohesion of the PBs may preferentially act through the mesen-

chymal population. This was demonstrated by showing that EMAPII reduced PB cohesivity by 6.5 dynes/cm, from 20 to 13.5 dyne/cm. Much of that decrease was related to a reduction in mesenchymal cell cohesion, as σ of that population was reduced from 20.1 to 10.6 dynes/cm, a reduction of 9.5 dynes/cm. This further confirms that EMAPII preferentially acts through the mesodermal cell population. The increased rate of compaction suggests that EMAPII, by decreasing overall cohesion, could, in principle, increase the motility of cells within a 3D tissue, the net effect essentially giving rise to a decrease in the effective viscosity of the system. This could, in turn, more easily drive cell rearrangement and reorganization in PBs.

EMAPII is not known to be involved in mediating tissue cohesion, yet our study showed this to be the case for lung tissue. We thus explored a potential molecular mechanism underlying EMAPII-associated decrease in PB cohesivity. In 3D tissues, intercellular cohesion has been shown to be mediated by both direct cadherin-based (30) and indirect integrin–FN–based interactions (10). Previous studies have indicated that FN matrix assembly is inhibited by EMAPII via a direct interaction with α5β1-integrin (24). We thus chose first to explore whether EMAPII altered α5-integrin–FN interaction, because we had previously demonstrated that blocking this interaction could give rise to a marked decrease in aggregate cohesivity (10). This proved to be the case in PBs, as blocking the α5β1 intracellular signaling interaction by a 70-kD FN fragment decreased PB cohesivity from approximately 20 dynes/cm to 13 dynes/cm, about the same degree of reduction resulting from EMAPII treatment. Moreover, treatment of PBs with the 70-kD fragment altered the rate of PB compaction in a dose-dependent manner, lower doses tending to accelerate compaction, and higher doses tending to delay it. This is logical, given that higher doses would disrupt the interaction past a point that would facilitate cell locomotion, effectively eliminating the required traction required for cell movement and compaction. Collectively, these data demonstrate a new role for EMAPII in mediating aggregate cohesion through an FN matrix–mediated adhesion system.

Alterations in the cohesivity in one of two interacting cell populations has been shown to markedly influence their spatial organization (41). Because PBs are essentially composed of cell populations derived from either the endoderm or mesoderm, we asked whether altering the relative cohesion between them could change their spatial organization. We used EMAPII to determine whether altering cohesion of the mesenchymal population influenced the spatial organization between the endodermal or mesodermal populations. EMAPII has been shown to disrupt distal lung formation by reducing the rate of neovascularization (1, 2, 22, 42–46). Various studies suggest that, during lung morphogenesis, disruption of vascular growth factors that induce pulmonary hypoplasia may arise from disruption of cell–cell interactions. Exploration of the interaction between morphogenesis and lung hypoplasia phenomena using the PBs allowed us to explore and manipulate the dynamic cell–cell interactions that facilitate lung development. Thus, PBs enabled us to identify factors that govern progressive distal alveolar structural and morphologic maturity and, ultimately, physiologic function for a better understanding of the pathologic progression. Loss of epithelial apical alignment and cellular organization suggests that cellular interactions with the ECM modulate epithelial–mesenchymal communications that are responsible for distal lung formation. Determination of the contribution that specific cellular populations make to fetal lung assembly and cohesion are the focus of our current studies.

Processed from the cell surface by proteolytic cleavage (29) to a mature roughly 22-kD form (27, 47, 48), EMAPII functions as a potent antiangiogenic peptide (28, 49). This is supported by its expression being inversely correlated with periods of vascularization (42, 50), and introduction of recombinant EMAPII in a murine allograft model of lung development profoundly disrupting alveolar capillary growth (2). Mechanistically, EMAPII functions by disrupting α5β1-integrin from binding to its extracellular ligand FN, resulting in delayed cell spreading, and disassembly of the cytoskeletal architecture of actin fiber networks and FN matrix (24). Although the impact of EMAPII on the pathologic progression of hypoplastic lung disease is well established, little is known about the mechanisms that contribute to distal lung hypoplasia. Analysis of EMAPII's ability to alter PB formation suggests that, in conjunction with an alteration in FN matrix deposition, subsequent epithelial polarity is disrupted, resulting in an alteration in cellular organization. Associated with the disruption of epithelial cell alignment of apical markers are epithelial cells cysts that were less complex, and collapsed into smaller aggregates. This is consistent with our previous observations in lung explants, where vessel inhibition resulted in an alteration in distal alveoli formation (2, 22) and the association of polarity with epithelial cell morphogenesis (25, 26). What is not clear in a 3D environment is whether epithelial morphogenesis is dependent on specific ECM components, such as FN or laminin, or is specifically altered by EMAPII. This area of investigation is part of our ongoing studies.

The observation that the anticohesive effects of EMAPII preferentially target the mesenchymal population suggests that, in a multi–cell type system such as the lung, factors can influence specific cell populations, and that this can give rise to a marked change in the overall biomechanical property of the tissue. This, in turn, could render that tissue either more susceptible to forces influencing cell organization, or by reducing overall cohesion, could make the tissue more amenable to infiltration by other cell types or by blood vessels.

In conclusion, our studies indicate that fetal lung has the unique property of self-assembly. Alterations in deposition of ECM result in the alteration of PB assembly, polarity, and cohesion. Furthermore, these findings support a role for the ECM and angiogenic mediators in the cell–cell interactions that modulate pulmonary morphogenesis, and highlight a new role for EMAPII as a regulator of indirect cell–cell cohesion. Understanding the role that ECM plays in the regulation of pulmonary morphogenesis and cellular cohesion can provide further insight into those factors that give rise to the lung as an organ capable of establishing an essential alveolar and vascular interface capable of oxygen exchange.

Author Disclosure: R.A.F received a sponsored grant from the National Institutes of Health (NIH) for more than $100,001; M.A.S. received a sponsored grant from NIH for more than $100,001; S.L. does not have a financial relationship with a commercial entity that has an interest in the subject of this manuscript; H.Z. does not have a financial relationship with a commercial entity that has an interest in the subject of this manuscript.

References

1. Zeng X, Wert SE, Federici R, Peters KG, Whitsett JA. VEGF enhances pulmonary vasculogenesis and disrupts lung morphogenesis *in vivo*. *Dev Dyn* 1998;211:215–227.
2. Schwarz MA, Zhang F, Gebb S, Starnes V, Warburton D. EMAP II inhibits lung neovascularization and airway epithelial morphogenesis. *Mech Dev* 2000;95:123–132.
3. Dickson MC, Martin JS, Cousins FM, Kulkarni AB, Karlsson S, Akhurst RJ. Defective haematopoiesis and vasculogenesis in transforming growth factor–beta 1 knock out mice. *Development* 1995;121:1845–1854.
4. Zhou L, Dey CR, Wert SE, Whitsett JA. Arrested lung morphogenesis in transgenic mice bearing an SP-C–TGF–beta 1 chimeric gene. *Dev Biol* 1996;175:227–238.

5. Schuger L, O'Shea KS, Nelson BB, Varani J. Organotypic arrangement of mouse embryonic lung cells on a basement membrane extract: involvement of laminin. *Development* 1990;110:1091–1099.
6. Mondrinos MJ, Koutzaki S, Jiwanmall E, Li M, Dechadarevian JP, Lelkes PI, Finck CM. Engineering three-dimensional pulmonary tissue constructs. *Tissue Eng* 2006;12:717–728.
7. Yu W, Fang X, Ewald A, Wong K, Hunt CA, Werb Z, Matthay MA, Mostov K. Formation of cysts by alveolar type II cells in three-dimensional culture reveals a novel mechanism for epithelial morphogenesis. *Mol Biol Cell* 2007;18:1693–1700.
8. Foty RA, Forgacs G, Pfleger CM, Steinberg MS. Liquid properties of embryonic tissues: measurement of interfacial tensions. *Phys Rev Lett* 1994;72:2298–2301.
9. Foty RA, Pfleger CM, Forgacs G, Steinberg MS. Surface tensions of embryonic tissues predict their mutual envelopment behavior. *Development* 1996;122:1611–1620.
10. Robinson EE, Foty RA, Corbett SA. Fibronectin matrix assembly regulates alpha5beta1-mediated cell cohesion. *Mol Biol Cell* 2004;15:973–981.
11. Robinson EE, Zazzali KM, Corbett SA, Foty RA. Alpha5beta1 integrin mediates strong tissue cohesion. *J Cell Sci* 2003;116:377–386.
12. Winters BS, Raj BK, Robinson EE, Foty RA, Corbett SA. Three-dimensional culture regulates RAF-1 expression to modulate fibronectin matrix assembly. *Mol Biol Cell* 2006;17:3386–3396.
13. Yang JM, O'Neill P, Jin W, Foty R, Medina DJ, Xu Z, Lomas M, Arndt GM, Tang Y, Nakada M, *et al.* Extracellular matrix metalloproteinase inducer (CD147) confers resistance of breast cancer cells to Anoikis through inhibition of Bim. *J Biol Chem* 2006;281:9719–9727.
14. Post M, Smith BT. Histochemical and immunocytochemical identification of alveolar type II epithelial cells isolated from fetal rat lung. *Am Rev Respir Dis* 1988;137:525–530.
15. Post M, Torday JS, Smith BT. Alveolar type II cells isolated from fetal rat lung organotypic cultures synthesize and secrete surfactant-associated phospholipids and respond to fibroblast-pneumonocyte factor. *Exp Lung Res* 1984;7:53–65.
16. Folkman J, Moscona A. Role of cell shape in growth control. *Nature* 1978;273:345–349.
17. Davies J, Rideal E. Interfacial phenomena. New York: Academic; 1963.
18. Steinberg MS. On the mechanism of tissue reconstruction by dissociated cells, III. Free energy relations and the reorganization of fused, heteronomic tissue fragments. *Proc Natl Acad Sci USA* 1962;48:1769–1776.
19. Schotz EM, Burdine RD, Julicher F, Steinberg MS, Heisenberg CP, Foty RA. Quantitative differences in tissue surface tension influence zebrafish germ layer positioning. *HFSP J* 2008;2:42–56.
20. Schuger L, Skubitz AP, Zhang J, Sorokin L, He L. Laminin alpha1 chain synthesis in the mouse developing lung: requirement for epithelial–mesenchymal contact and possible role in bronchial smooth muscle development. *J Cell Biol* 1997;139:553–562.
21. Schuger L, Varani J, Killen PD, Skubitz AP, Gilbride K. Laminin expression in the mouse lung increases with development and stimulates spontaneous organotypic rearrangement of mixed lung cells. *Dev Dyn* 1992;195:43–54.
22. Schwarz MA, Wan Z, Liu J, Lee MK. Epithelial–mesenchymal interactions are linked to neovascularization. *Am J Respir Cell Mol Biol* 2004;30:784–792.
23. Quintos-Alagheband ML, White CW, Schwarz MA. Potential role for antiangiogenic proteins in the evolution of bronchopulmonary dysplasia. *Antioxid Redox Signal* 2004;6:137–145.
24. Schwarz MA, Zheng H, Liu J, Corbett S, Schwarz RE. Endothelial–monocyte activating polypeptide II alters fibronectin based endothelial cell adhesion and matrix assembly via alpha5 beta1 integrin. *Exp Cell Res* 2005;311:229–239.
25. Wang AZ, Ojakian GK, Nelson WJ. Steps in the morphogenesis of a polarized epithelium. II. Disassembly and assembly of plasma membrane domains during reversal of epithelial cell polarity in multicellular epithelial (MDCK) cysts. *J Cell Sci* 1990;95(Pt 1):153–165.
26. Wang AZ, Ojakian GK, Nelson WJ. Steps in the morphogenesis of a polarized epithelium. I. Uncoupling the roles of cell–cell and cell–substratum contact in establishing plasma membrane polarity in multicellular epithelial (MDCK) cysts. *J Cell Sci* 1990;95(Pt 1):137–151.
27. Kao J, Houck K, Fan Y, Haehnel I, Libutti SK, Kayton ML, Grikscheit T, Chabot J, Nowygrod R, Greenberg S, *et al.* Characterization of a novel tumor-derived cytokine: endothelial–monocyte activating polypeptide II. *J Biol Chem* 1994;269:25106–25119.
28. Schwarz MA, Kandel J, Brett G, Li J, Hayward J, Schwarz RE, Chappey O, Wautier J, Chabot J, Lo Gerfo P, *et al.* Endothelial-monocyte activating polypeptide II, a novel antitumor cytokine that suppresses primary and metastatic tumor growth, and induces apoptosis in growing endothelial cells. *J Exp Med* 1999;190:341–353.
29. Liu J, Schwarz MA. Identification of protease-sensitive sites in human endothelial–monocyte activating polypeptide II protein. *Exp Cell Res* 2006;312:2231–2237.
30. Foty RA, Steinberg MS. Cadherin-mediated cell–cell adhesion and tissue segregation in relation to malignancy. *Int J Dev Biol* 2004;48:397–409.
31. Schwartz MA, Ginsberg MH. Networks and crosstalk: integrin signalling spreads. *Nat Cell Biol* 2002;4:E65–E68.
32. Chandramouly G, Abad PC, Knowles DW, Lelievre SA. The control of tissue architecture over nuclear organization is crucial for epithelial cell fate. *J Cell Sci* 2007;120:1596–1606.
33. Jia D, Dajusta D, Foty RA. Tissue surface tensions guide in vitro self-assembly of rodent pancreatic islet cells. *Dev Dyn* 2007;236:2039–2049.
34. Kelm JM, Ittner LM, Born W, Djonov V, Fussenegger M. Self-assembly of sensory neurons into ganglia-like microtissues. *J Biotechnol* 2006;121:86–101.
35. Perez-Pomares JM, Foty RA. Tissue fusion and cell sorting in embryonic development and disease: Biomedical implications. *Bioessays* 2006;28:809–821.
36. Foty RA, Corbett SA, Schwarzbauer JE, Steinberg MS. Dexamethasone up-regulates cadherin expression and cohesion of HT-1080 human fibrosarcoma cells. *Cancer Res* 1998;58:3586–3589.
37. Foty RA, Steinberg MS. Measurement of tumor cell cohesion and suppression of invasion by E- or P-cadherin. *Cancer Res* 1997;57:5033–5036.
38. Jakab K, Neagu A, Mironov V, Markwald RR, Forgacs G. Engineering biological structures of prescribed shape using self-assembling multicellular systems. *Proc Natl Acad Sci USA* 2004;101:2864–2869.
39. Kelm JM, Djonov V, Ittner LM, Fluri D, Born W, Hoerstrup SP, Fussenegger M. Design of custom-shaped vascularized tissues using microtissue spheroids as minimal building units. *Tissue Eng* 2006;12:2151–2160.
40. Neagu A, Jakab K, Jamison R, Forgacs G. Role of physical mechanisms in biological self-organization. *Phys Rev Lett* 2005;95:178104.
41. Duguay D, Foty RA, Steinberg MS. Cadherin-mediated cell adhesion and tissue segregation: qualitative and quantitative determinants. *Dev Bio* 2003;253:309–323.
42. Schwarz M, Lee M, Zhang F, Zhao J, Jin Y, Smith S, Bhuva J, Stern D, Warburton D, Starnes V. EMAP II: a modulator of neovascularization in the developing lung. *Am J Physiol* 1999;276:L365–L375.
43. DeLisser HM, Helmke BP, Cao G, Egan PM, Taichman D, Fehrenbach M, Zaman A, Cui Z, Mohan GS, Baldwin HS, *et al.* Loss of PECAM-1 function impairs alveolarization. *J Biol Chem* 2006;281:8724–8731.
44. Jakkula M, Le Cras TD, Gebb S, Hirth KP, Tuder RM, Voelkel NF, Abman SH. Inhibition of angiogenesis decreases alveolarization in the developing rat lung. *Am J Physiol Lung Cell Mol Physiol* 2000;279:L600–L607.
45. Le Cras TD, Markham NE, Tuder RM, Voelkel NF, Abman SH. Treatment of newborn rats with a VEGF receptor inhibitor causes pulmonary hypertension and abnormal lung structure. *Am J Physiol Lung Cell Mol Physiol* 2002;283:L555–L562.
46. Lin Y, Zhang S, Rehn M, Itaranta P, Tuukkanen J, Heljasvaara R, Peltoketo H, Pihlajaniemi T, Vainio S. Induced repatterning of type XVIII collagen expression in ureter bud from kidney to lung type: association with sonic hedgehog and ectopic surfactant protein C. *Development* 2001;128:1573–1585.
47. Kao J, Fan YG, Haehnel I, Clauss M, Stern D. Endothelial–monocyte activating polypeptides (EMAPs): tumor derived mediators which activate the host inflammatory response. *Behring Inst Mitt* 1993;92:92–106.
48. Kao J, Ryan J, Brett G, Chen J, Shen H, Fan YG, Godman G, Familletti PC, Wang F, Pan YC, *et al.* Endothelial monocyte-activating polypeptide II: a novel tumor-derived polypeptide that activates host-response mechanisms. *J Biol Chem* 1992;267:20239–20247.
49. Schwarz RE, Schwarz MA. *In vivo* therapy of local tumor progression by targeting vascular endothelium with EMAP-II. *J Surg Res* 2004;120:64–72.
50. Zhang F, Schwarz MA. Temporo-spatial distribution of endothelial-monocyte activating polypeptide II, an anti-angiogenic protein, in the mouse embryo. *Dev Dyn* 2000;218:490–498.